


Time evolution of coherent wave propagation and spin relaxation in spin-orbit-coupled systemsMasataka Kakoi^{✉*} and Keith Slevin^{✉†}*Department of Physics, Osaka University, 1-1 Machikaneyama-cho, Toyonaka, Osaka 560-0043, Japan* (Received 7 November 2023; accepted 12 February 2024; published 4 March 2024)

We investigate, both numerically and analytically, the time evolution of a particle in an initial plane-wave state as it is subject to elastic scattering in a two-dimensional disordered system with Rashba spin-orbit coupling (SOC). In the analytic calculation, we treat the SOC nonperturbatively and the disorder perturbatively using the diffuson and the cooperon. We calculate the time dependence of coherent backscattering as a function of the strength of the SOC. We identify weak and strong SOC regimes and give the relevant time and energy scales in each case. By studying the time dependence of the anisotropy of the disorder-averaged momentum distribution, we identify the spin-relaxation time. We find a crossover from D'yakonov-Perel' spin relaxation for weak SOC to Elliot-Yafet-like behavior for strong SOC.

DOI: [10.1103/PhysRevA.109.033303](https://doi.org/10.1103/PhysRevA.109.033303)**I. INTRODUCTION**

Cold atomic gases have unique features that are advantageous for research on coherent wave propagation in disordered systems. Experiments can be performed in a regime where the gas is noninteracting. The gas can be put into a specified initial state and the subsequent time evolution of the spatial and momentum distributions of the atoms can be measured. The gas can be subjected to a random potential by applying laser speckle. Observations [1,2] of coherent backscattering (CBS) and of Anderson localization [3–5] have been performed in this way. Further developments of experimental technique, e.g., bichromatic speckle [6], promise quantitative measurement of the Anderson transition in speckle potentials.

An alternative approach is to subject the gas to a quasiperiodic modulation to realize a quantum kicked rotor with a quasiperiodic kick. This system exhibits dynamical localization, an analog of Anderson localization in momentum space. In this way, the analog of the three-dimensional Anderson transition has been observed [7]. The critical exponent of the transition has been measured [8] and found to be in good agreement with numerical finite-time-scaling studies of the quantum kicked rotor [9] and with finite-size-scaling studies of Anderson's model of localization [10,11]. Other signatures of Anderson localization, namely, coherent forward scattering and the quantum boomerang effect, have been proposed theoretically [12,13] and then subsequently observed [14,15] in the cold-atom quantum kicked rotor.

Coherent backscattering results from interference between time-reversed scattering processes. This interference is usually constructive and is manifest in an enhanced probability, ideally by a factor of 2, for a wave to be scattered in the

direction opposite to that of the incident wave. This has been observed in optics [16,17], acoustics [18], and cold atoms [1,2]. In solid-state physics, it is manifest in the weak localization effect [19]. In cold atoms, the constructive interference of time-reversed states leads to the emergence of characteristic structures in the disorder-averaged momentum distribution [20,21].

Spin-orbit coupling (SOC) is well known in atomic and solid-state physics. It involves the coupling of an electron's spin with its orbital motion. The importance of SOC is that it breaks spin-rotation symmetry while preserving time-reversal symmetry. In a system with both time-reversal symmetry and spin-rotation symmetry, the electron spin plays no role in the dynamics and the operation of time reversal corresponds to reversing the electron's momentum. In a system with time-reversal symmetry but where spin-rotation symmetry is broken by SOC, the operation of time reversal also involves reversing the electron's spin. This has a dramatic effect on the interference between time-reversed processes, changing it from constructive to destructive. In solid-state physics this is manifested in the weak antilocalization effect [19,22]. Synthetic SOC has been realized experimentally in both Bose and Fermi gases [23–27]. This brings into prospect experiments that combine synthetic SOC with random potentials and this has stimulated recent theoretical work [28–33].

To make clear the importance of SOC for interference between time-reversed scattering processes, consider a gas of electrons in the independent-particle approximation described by a single-particle Hamiltonian H . Let us suppose that H has time-reversal symmetry, i.e., that H commutes with a time-reversal operator T ,

$$[H, T] = 0. \quad (1)$$

If H has spin-rotation symmetry, we have $T^2 = +1$, since reversing the momentum twice leaves the momentum unchanged. If spin-rotation symmetry is broken by SOC, we have $T^2 = -1$. This is because reversing the electron's spin

*kakoi@presto.phys.sci.osaka-u.ac.jp

†slevin.keith.sci@osaka-u.ac.jp

TABLE I. Energy scales and time scales governing the time-dependent behavior for the weak and strong SOC limits. Here τ is the scattering time and Δ is the spin splitting induced by SOC.

Scale	Weak SOC	Strong SOC
Energy	$\Delta \ll \hbar/\tau$	$\Delta \gg \hbar/\tau$
Time	$\tau, \hbar^2/\tau\Delta^2$	$\tau, \hbar/\Delta$

twice introduces a change of sign. Starting from Eq. (1) and assuming $T^2 = -1$, we find that the probability of scattering into a time-reversed state is zero (see Appendix A),

$$\langle T\psi_0 | \exp(-iHt) | \psi_0 \rangle = 0, \quad (2)$$

for any arbitrary initial state $|\psi_0\rangle$ and for all times t . Note that this does not mean that scattering into a state with opposite momentum cannot occur, but rather that scattering into a state with opposite momentum and opposite spin cannot occur.

In this paper we consider the time evolution of an initial plane-wave state with wave vector \mathbf{k}_0 resulting from elastic scattering by the random potential. By treating the SOC nonperturbatively and disorder perturbatively using a diagrammatic perturbation theory, we identify weak and strong SOC regimes. In Table I we tabulate the corresponding time and energy scales. In Fig. 1, in a regime of weak SOC, we show the buildup of the diffusive ring on the order of the scattering time τ , the enhancement of backscattering on times of the order of several τ , and the reduction of backscattering at much longer times. As can be seen in Figs. 2(d)–2(f), we obtain good agreement between numerical and analytical results without any fitting parameters for the entire range from weak SOC to strong SOC.

Spin-orbit coupling also leads to significant anisotropy in the disorder-averaged momentum distribution. This is seen not only for strong SOC, as in Figs. 3, 10, and 11, but also for weak SOC when the disorder-averaged momentum distribution is spin resolved as in Fig. 12. This anisotropy relaxes at sufficiently long times due to spin relaxation. By studying this, we are able to determine the spin-relaxation time and investigate the crossover from D'yakonov-Perel' spin relaxation for weak SOC to Elliot-Yafet-like behavior for strong SOC.

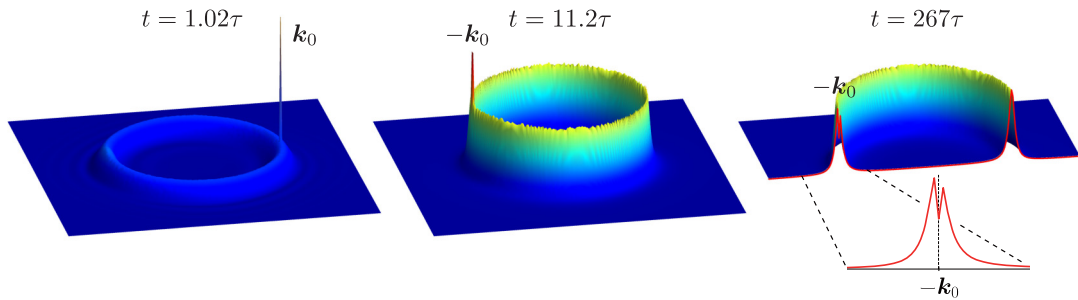


FIG. 1. Simulation of the time evolution of a plane wave with initial wave vector $\mathbf{k}_0 = (k_0, 0)$ in two-dimensional systems with weak disorder and weak SOC. We use the Ando model [34], as described by Eq. (4), with $\varphi = \pi/1024$ and a disorder strength of $W = 1$. The disorder-averaged momentum distribution $n(\mathbf{k}, t)$ is estimated by sampling $2^{13} = 8192$ disorder realizations. An isotropic diffusive background ring due to elastic scattering is observed with a crossover from enhanced backscattering at a time of several τ to reduced backscattering at much longer times.

II. MODEL

In this study we use the Ando model [34], which is a tight-binding model with Rashba-type SOC defined on a square lattice, with the lattice constant taken as the unit of length. The Hamiltonian in the spin basis

$$|\uparrow\rangle = \begin{pmatrix} 1 \\ 0 \end{pmatrix}, \quad |\downarrow\rangle = \begin{pmatrix} 0 \\ 1 \end{pmatrix} \quad (3)$$

is given by

$$H_0 = -t_{\text{hop}} \sum_{\mathbf{r}} \sum_{\sigma, \sigma'} [(T_x)_{\sigma\sigma'} c_{\mathbf{r}+\mathbf{e}_x, \sigma}^\dagger c_{\mathbf{r}, \sigma'} + (T_y)_{\sigma\sigma'} c_{\mathbf{r}+\mathbf{e}_y, \sigma}^\dagger c_{\mathbf{r}, \sigma'} + \text{H.c.}] \quad (4)$$

Here

$$T_x = \begin{pmatrix} t_1 & t_2 \\ -t_2 & t_1 \end{pmatrix}, \quad T_y = \begin{pmatrix} t_1 & -it_2 \\ -it_2 & t_1 \end{pmatrix}, \quad (5)$$

with

$$t_1 = \cos \varphi, \quad t_2 = \sin \varphi. \quad (6)$$

Also, $c_{\mathbf{r}, \sigma}^\dagger$ and $c_{\mathbf{r}, \sigma}$ are creation and annihilation operators, respectively, at site \mathbf{r} and spin σ , and \mathbf{e}_x and \mathbf{e}_y are lattice vectors. We take t_{hop} and \hbar/t_{hop} as the units of energy and time, respectively.

We consider square systems with linear size L . The Hamiltonian (4) may then be expressed in momentum space as

$$H_0 = \sum_{\sigma, \sigma'} \sum_{\mathbf{k}} [H_0(\mathbf{k})]_{\sigma\sigma'} c_{\mathbf{k}, \sigma}^\dagger c_{\mathbf{k}, \sigma'}, \quad (7)$$

where the summation is over spin and the appropriate allowed values of \mathbf{k} in the first Brillouin zone and

$$H_0(\mathbf{k}) = \begin{pmatrix} -2t_1(\cos k_x + \cos k_y) & 2t_2(-i \sin k_x - \sin k_y) \\ 2t_2(i \sin k_x - \sin k_y) & -2t_1(\cos k_x + \cos k_y) \end{pmatrix}. \quad (8)$$

The Hamiltonian (8) is diagonalized by the following momentum-coupled spin basis, which we refer to in what follows as the \pm basis:

$$|\mathbf{k}, \pm\rangle = |\mathbf{k}\rangle \otimes \left(\frac{|\uparrow\rangle - e^{-i\theta(\mathbf{k})} |\downarrow\rangle}{\sqrt{2}} \right), \quad (9)$$

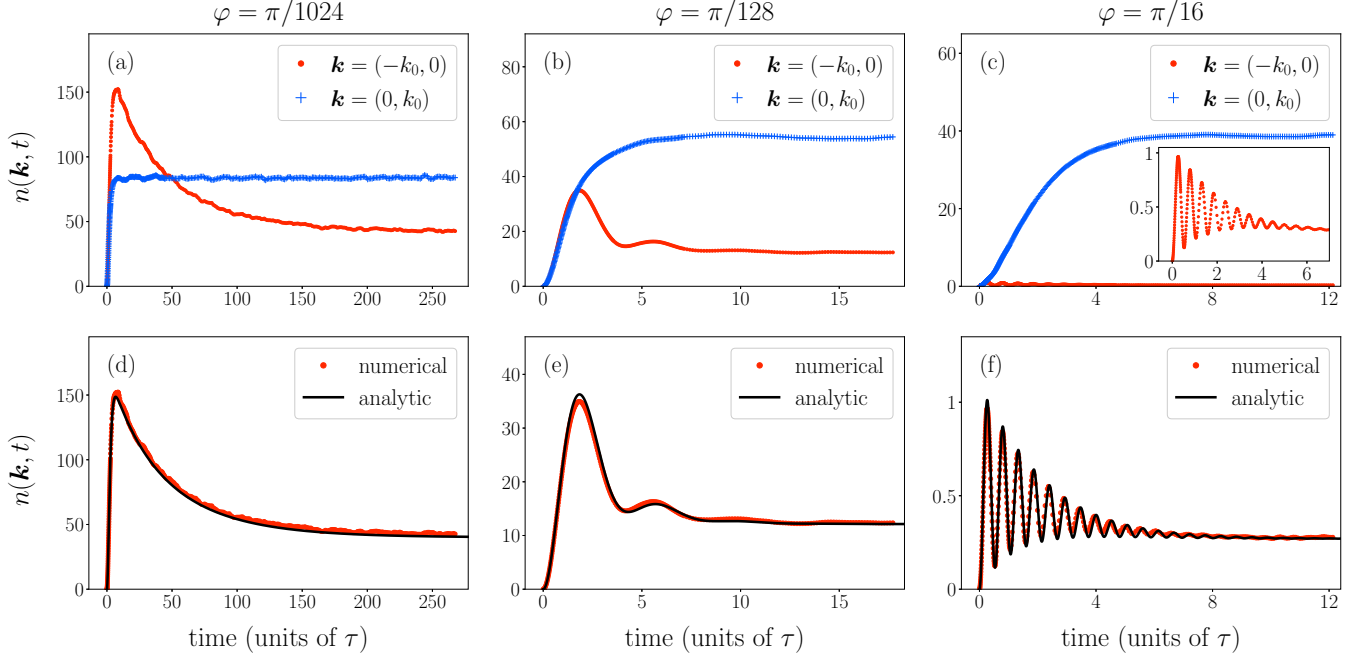


FIG. 2. [(a)–(c)] Comparison of the time dependence of the disorder-averaged momentum distribution $n(\mathbf{k}, t)$ at two points $\mathbf{k} = (-k_0, 0)$ (red points) and $\mathbf{k} = (0, k_0)$ (blue crosses) estimated by sampling 8192 disorder realizations. The disorder strength is fixed at $W = 1$ for all cases, while the strength of the SOC varies: $\varphi = \pi/1024$ for weak SOC, $\varphi = \pi/128$ for intermediate SOC, and $\varphi = \pi/16$ for strong SOC. [(d)–(f)] Comparison between the disorder-averaged momentum distribution at $\mathbf{k} = (-k_0, 0)$ obtained in the simulation and that obtained from a diagrammatic expansion (solid line): (d) Eq. (58) and (e) and (f) Eq. (59).

$$|\mathbf{k}, -\rangle = |\mathbf{k}\rangle \otimes \left(-\frac{e^{i\theta(\mathbf{k})}|\uparrow\rangle + |\downarrow\rangle}{\sqrt{2}} \right). \quad (10)$$

Here $\theta(\mathbf{k})$ is a real value for any wave vector \mathbf{k} and satisfies

$$e^{i\theta(\mathbf{k})} = \frac{i \sin k_x + \sin k_y}{\sqrt{\sin^2 k_x + \sin^2 k_y}}. \quad (11)$$

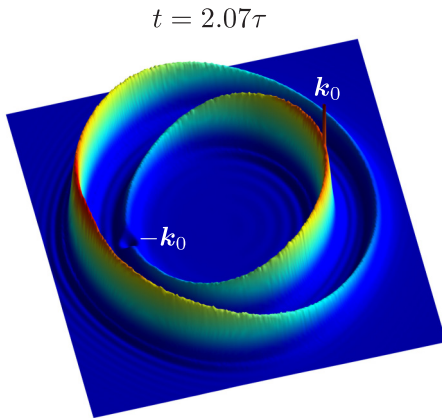


FIG. 3. Disorder-averaged momentum distribution for strong SOC. The model parameters are $\varphi = \pi/16$ and $W = 1$. At long times, the anisotropy of the diffusive background rings disappears. A view of the cross section is presented in Fig. 11(a).

The state $|\mathbf{k}, +\rangle$ is equal to the time-reversed state of $|\mathbf{k}, -\rangle$ up to a phase factor,¹

$$\begin{aligned} T|\mathbf{k}, +\rangle &= i\sigma_y K|\mathbf{k}, +\rangle \\ &= |\mathbf{k}, -\rangle \otimes \left(-\frac{|\downarrow\rangle + e^{i\theta(\mathbf{k})}|\uparrow\rangle}{\sqrt{2}} \right) \\ &= e^{i\theta(\mathbf{k})}|\mathbf{k}, -\rangle, \end{aligned} \quad (12)$$

where σ_y is the Pauli matrix, K is the complex conjugation, and we used the relation $e^{i\theta(-\mathbf{k})} = -e^{i\theta(\mathbf{k})}$. Also, the corresponding relationship holds for $|\mathbf{k}, -\rangle$ and $|\mathbf{k}, +\rangle$,

$$T|\mathbf{k}, -\rangle = e^{-i\theta(\mathbf{k})}|\mathbf{k}, -\rangle. \quad (13)$$

The eigenstates (9) and (10) have eigenenergies

$$\begin{aligned} E_{\pm}(\mathbf{k}) &= -2t_1(\cos k_x + \cos k_y) \\ &\quad \pm 2t_2\sqrt{\sin^2 k_x + \sin^2 k_y}, \end{aligned} \quad (14)$$

respectively. In Fig. 4 we show the band structure of the Ando model, where the spin splitting into upper and lower branches due to SOC is visible.

¹We note that the phase factors in Eqs. (12) and (13) are to some extent arbitrary, as the eigenvectors (9) and (10) and the time-reversal operator T are only defined up to arbitrary complex phase factors. These phase factors do not affect the subsequent calculations.

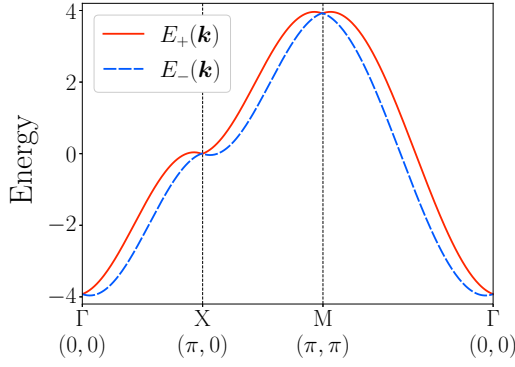


FIG. 4. Band structure of the Ando model with the parameters $t_1 = \cos \varphi$, $t_2 = \sin \varphi$, and $\varphi = \pi/16$. As t_2 increases, the spin splitting into upper branch $E_+(\mathbf{k})$ and lower branch $E_-(\mathbf{k})$ becomes larger.

We suppose a spin-independent random potential of the form

$$V = \sum_{\mathbf{r}} \sum_{\sigma} w_{\mathbf{r}} c_{\mathbf{r},\sigma}^{\dagger} c_{\mathbf{r},\sigma}, \quad (15)$$

where $w_{\mathbf{r}}$ are independently and identically distributed random variables with uniform distribution on the interval $[-W/2, W/2]$. The potential distribution is uncorrelated and translationally invariant. Therefore, the disorder-averaged Green's function is also translationally invariant, i.e.,

$$\overline{G}^{R(A)}(\mathbf{r}, \mathbf{r}', \varepsilon) = \overline{G}^{R(A)}(\mathbf{r} - \mathbf{r}', \varepsilon), \quad (16)$$

and is diagonal with respect to the wave vector [35],

$$\overline{G}^{R(A)}(\mathbf{k}, \mathbf{k}', \varepsilon) = \overline{G}^{R(A)}(\mathbf{k}, \varepsilon) \delta_{\mathbf{k},\mathbf{k}'}. \quad (17)$$

Here R stands for retarded and A stands for advanced. In addition, if the random potential is spin independent and

has short-range correlations, as in this paper, the disorder-averaged Green's function is a diagonal matrix in the \pm basis,

$$\overline{G}^{R(A)}(\mathbf{k}, \varepsilon) = g_+^{R(A)}(\mathbf{k}, \varepsilon) |\mathbf{k}, +\rangle \langle \mathbf{k}, +| + g_-^{R(A)}(\mathbf{k}, \varepsilon) |\mathbf{k}, -\rangle \langle \mathbf{k}, -|. \quad (18)$$

The diagonal elements are

$$g_{\pm}^R(\mathbf{k}, \varepsilon) = \frac{1}{\varepsilon - E_{\pm}(\mathbf{k}) + i/2\tau}, \quad (19)$$

$$g_{\pm}^A(\mathbf{k}, \varepsilon) = \frac{1}{\varepsilon - E_{\pm}(\mathbf{k}) - i/2\tau}. \quad (20)$$

The detailed calculation is presented in Appendix B.

III. DIAGRAMMATIC CALCULATION

In this study we consider the time evolution of the disorder-averaged momentum distribution. The disorder-averaged momentum distribution at wave vector \mathbf{k} and time t , given an initial state $|\psi_0\rangle$, is

$$n(\mathbf{k}, t) = \overline{\langle \psi(t) | (|\mathbf{k}, +\rangle \langle \mathbf{k}, +| + |\mathbf{k}, -\rangle \langle \mathbf{k}, -|) | \psi(t) \rangle} := n_+(\mathbf{k}, t) + n_-(\mathbf{k}, t), \quad (21)$$

where

$$|\psi(t)\rangle = e^{-i(H_0+V)t} |\psi_0\rangle. \quad (22)$$

The branch resolved components $n_+(\mathbf{k})$ and $n_-(\mathbf{k})$ can be expressed as² [20,36–38]

$$n_{\pm}(\mathbf{k}, t) = \int_{-\infty}^{\infty} \frac{d\varepsilon}{2\pi} \int_{-\infty}^{\infty} \frac{d\omega}{2\pi} e^{-i\omega t} \Phi_{\pm}(\mathbf{k}, \varepsilon, \omega), \quad (23)$$

where

$$\Phi_{\pm}(\mathbf{k}, \varepsilon, \omega) = \sum_{a,b=\pm} \int \frac{d^2\mathbf{k}' d^2\mathbf{k}''}{(2\pi)^4} \overline{\langle \mathbf{k}, \pm | G^R\left(\varepsilon + \frac{\omega}{2}\right) | \mathbf{k}', a \rangle \langle \mathbf{k}'', b | G^A\left(\varepsilon - \frac{\omega}{2}\right) | \mathbf{k}, \pm \rangle \langle \mathbf{k}', a | \psi_0 \rangle \langle \psi_0 | \mathbf{k}'', b \rangle}. \quad (24)$$

To avoid confusion, from now on, we associate latin subscripts with the \pm basis and greek subscripts with the spin basis, i.e., a and b represent $+$ or $-$, while α, β , and so on represent \uparrow or \downarrow . As the initial state, we take the plane wave that is an eigenstate of H_0 given in Eq. (4) in the upper branch whose energy is $E_+(\mathbf{k}_0)$,

$$|\psi_0\rangle = |\mathbf{k}_0, +\rangle. \quad (25)$$

Substituting the initial state (25) into Eq. (24), performing the integration on \mathbf{k}' and \mathbf{k}'' , and summing over a and b , we obtain

$$\Phi_{\pm}(\mathbf{k}, \varepsilon, \omega) = \overline{\langle \mathbf{k}, \pm | G^R\left(\varepsilon + \frac{\omega}{2}\right) | \mathbf{k}_0, + \rangle \langle \mathbf{k}_0, + | G^A\left(\varepsilon - \frac{\omega}{2}\right) | \mathbf{k}, \pm \rangle}. \quad (26)$$

Equation (26) includes contributions from all scattering processes, but we approximate these by retaining only the contributions from the ladder diagram (diffuson) and the maximally crossed diagram (cooperon) [20,35],

$$n_{\pm}(\mathbf{k}, t) \simeq \int_{-\infty}^{\infty} \frac{d\varepsilon}{2\pi} \int_{-\infty}^{\infty} \frac{d\omega}{2\pi} e^{-i\omega t} [\Phi_{\pm}^0(\mathbf{k}, \varepsilon, \omega) + \Phi_{\pm}^D(\mathbf{k}, \varepsilon, \omega) + \Phi_{\pm}^C(\mathbf{k}, \varepsilon, \omega)], \quad (27)$$

where

$$\Phi_{\pm}^0(\mathbf{k}, \varepsilon, \omega) = g_+^R\left(\mathbf{k}_0, \varepsilon + \frac{\omega}{2}\right) g_+^A\left(\mathbf{k}_0, \varepsilon - \frac{\omega}{2}\right) \delta(\mathbf{k} - \mathbf{k}_0) \delta_{\pm,+}, \quad (28)$$

²In Sec. III, all sums with respect to \mathbf{k}' are replaced by integrals

$$\Phi_{\pm}^D(\mathbf{k}, \varepsilon, \omega) = g_{\pm}^R\left(\mathbf{k}, \varepsilon + \frac{\omega}{2}\right) g_{\pm}^A\left(\mathbf{k}, \varepsilon - \frac{\omega}{2}\right) \Gamma_{\pm\pm,++}^D(\mathbf{k}, \mathbf{k}_0, \varepsilon, \omega) g_{\pm}^R\left(\mathbf{k}_0, \varepsilon + \frac{\omega}{2}\right) g_{\pm}^A\left(\mathbf{k}_0, \varepsilon - \frac{\omega}{2}\right), \quad (29)$$

$$\Phi_{\pm}^C(\mathbf{k}, \varepsilon, \omega) = g_{\pm}^R\left(\mathbf{k}, \varepsilon + \frac{\omega}{2}\right) g_{\pm}^A\left(\mathbf{k}, \varepsilon - \frac{\omega}{2}\right) \Gamma_{\pm\pm,++}^C(\mathbf{k}, \mathbf{k}_0, \varepsilon, \omega) g_{\pm}^R\left(\mathbf{k}_0, \varepsilon + \frac{\omega}{2}\right) g_{\pm}^A\left(\mathbf{k}_0, \varepsilon - \frac{\omega}{2}\right). \quad (30)$$

The operators Γ^D and Γ^C in the \pm basis can be projected to the operators Γ^D and Γ^C in the spin basis using unitary operators with

$$U_{\alpha\beta,ab}(\mathbf{k}) = \langle \mathbf{k}, \alpha | \mathbf{k}, a \rangle \langle \mathbf{k}, b | \mathbf{k}, \beta \rangle \quad (31)$$

as elements. The projection is represented in matrix representation as

$$\Gamma^D(\mathbf{k}, \mathbf{k}', \varepsilon, \omega) = U^\dagger(\mathbf{k}) \Gamma^D(\mathbf{0}, \varepsilon, \omega) U(\mathbf{k}'), \quad (32)$$

$$\Gamma^C(\mathbf{k}, \mathbf{k}', \varepsilon, \omega) = U^\dagger(\mathbf{k}) \Gamma^C(\mathbf{k} + \mathbf{k}', \varepsilon, \omega) U(\mathbf{k}'), \quad (33)$$

where $U(\mathbf{k})$ is a Hermitian unitary matrix

$$U(\mathbf{k}) = \frac{1}{2} \begin{pmatrix} 1 & -e^{i\theta(\mathbf{k})} & -e^{-i\theta(\mathbf{k})} & 1 \\ -e^{-i\theta(\mathbf{k})} & -1 & e^{-2i\theta(\mathbf{k})} & e^{-i\theta(\mathbf{k})} \\ -e^{i\theta(\mathbf{k})} & e^{2i\theta(\mathbf{k})} & -1 & e^{i\theta(\mathbf{k})} \\ 1 & e^{i\theta(\mathbf{k})} & e^{-i\theta(\mathbf{k})} & 1 \end{pmatrix}. \quad (34)$$

The diagrams of Γ^D and Γ^C are shown in Fig. 5. In the absence of SOC, time-reversal symmetry ensures that reversing the direction of the arrows yields the same result. Consequently, in the long-time limit, the contributions of the diffuson and the cooperon become equal at $\mathbf{k} = -\mathbf{k}_0$. However, in the present discussion, the direction of the arrows carries significant meaning. For Γ^D and Γ^C in the spin basis, Bethe-Salpeter equations

$$\Gamma_{\alpha\beta,\gamma\delta}^D(\mathbf{q}, \varepsilon, \omega) = \gamma_0 \delta_{\alpha,\gamma} \delta_{\beta,\delta} + \gamma_0 \sum_{\mu,\nu} \Pi_{\alpha\beta,\mu\nu}^D(\mathbf{q}, \varepsilon, \omega) \Gamma_{\mu\nu,\gamma\delta}^D(\mathbf{q}, \varepsilon, \omega), \quad (35)$$

$$\Gamma_{\alpha\delta,\gamma\beta}^C(\mathbf{q}, \varepsilon, \omega) = \gamma_0^2 \Pi_{\alpha\delta,\gamma\beta}^C(\mathbf{q}, \varepsilon, \omega) + \gamma_0 \sum_{\mu,\nu} \Pi_{\alpha\delta,\mu\nu}^C(\mathbf{q}, \varepsilon, \omega) \Gamma_{\mu\nu,\gamma\beta}^C(\mathbf{q}, \varepsilon, \omega) \quad (36)$$

hold. For the cooperon, Eq. (36) is obtained by “twisting” the Γ^C diagram in Fig. 5. Here Π^D and Π^C are

$$\Pi_{\alpha\beta,\gamma\delta}^D(\mathbf{q}, \varepsilon, \omega) = \int \frac{d^2\mathbf{k}''}{(2\pi)^2} \bar{\mathcal{G}}_{\alpha\gamma}^R\left(\mathbf{k}'', \varepsilon + \frac{\omega}{2}\right) \bar{\mathcal{G}}_{\delta\beta}^A\left(\mathbf{q} + \mathbf{k}'', \varepsilon - \frac{\omega}{2}\right), \quad (37)$$

$$\Pi_{\alpha\beta,\gamma\delta}^C(\mathbf{q}, \varepsilon, \omega) = \int \frac{d^2\mathbf{k}''}{(2\pi)^2} \bar{\mathcal{G}}_{\alpha\gamma}^R\left(\mathbf{k}'', \varepsilon + \frac{\omega}{2}\right) \bar{\mathcal{G}}_{\beta\delta}^A\left(\mathbf{q} - \mathbf{k}'', \varepsilon - \frac{\omega}{2}\right), \quad (38)$$

where $\bar{\mathcal{G}}_{\alpha\beta}^{R(A)}$ is the element of the disorder-averaged Green's function in the spin basis

$$\bar{\mathcal{G}}^{R(A)}(\mathbf{q}, \varepsilon) = \frac{1}{2} \begin{pmatrix} g_+^{R(A)}(\mathbf{q}, \varepsilon) + g_-^{R(A)}(\mathbf{q}, \varepsilon) & -e^{-i\theta(\mathbf{q})}(g_+^{R(A)}(\mathbf{q}, \varepsilon) - g_-^{R(A)}(\mathbf{q}, \varepsilon)) \\ -e^{i\theta(\mathbf{q})}(g_+^{R(A)}(\mathbf{q}, \varepsilon) - g_-^{R(A)}(\mathbf{q}, \varepsilon)) & g_+^{R(A)}(\mathbf{q}, \varepsilon) + g_-^{R(A)}(\mathbf{q}, \varepsilon) \end{pmatrix} \quad (39)$$

and

$$\gamma_0 = \frac{1}{\pi \rho \tau}. \quad (40)$$

Here ρ is the density of states.

When considering $\mathbf{k} = -\mathbf{k}_0$ in Eq. (27), it is apparent that by using Eqs. (32) and (33), it is sufficient to calculate $\Gamma^D(\mathbf{0}, \varepsilon, \omega)$ and $\Gamma^C(\mathbf{0}, \varepsilon, \omega)$, or equivalently $\Pi^D(\mathbf{0}, \varepsilon, \omega)$ and $\Pi^C(\mathbf{0}, \varepsilon, \omega)$. Performing the integration in Eqs. (37) and (38) taking into account factors such as $e^{i\theta(-\mathbf{k})} = -e^{i\theta(\mathbf{k})}$ and $e^{2i\theta(k_x, k_y)} = -e^{2i\theta(k_y, -k_x)}$, several terms cancel out and we obtain

$$\Pi^D(\mathbf{0}, \varepsilon, \omega) = \begin{pmatrix} \Pi_1 & 0 & 0 & \Pi_2 \\ 0 & \Pi_1 & 0 & 0 \\ 0 & 0 & \Pi_1 & 0 \\ \Pi_2 & 0 & 0 & \Pi_1 \end{pmatrix}, \quad (41)$$

$$\Pi^C(\mathbf{0}, \varepsilon, \omega) = \begin{pmatrix} \Pi_1 & 0 & 0 & 0 \\ 0 & \Pi_1 & -\Pi_2 & 0 \\ 0 & -\Pi_2 & \Pi_1 & 0 \\ 0 & 0 & 0 & \Pi_1 \end{pmatrix}, \quad (42)$$

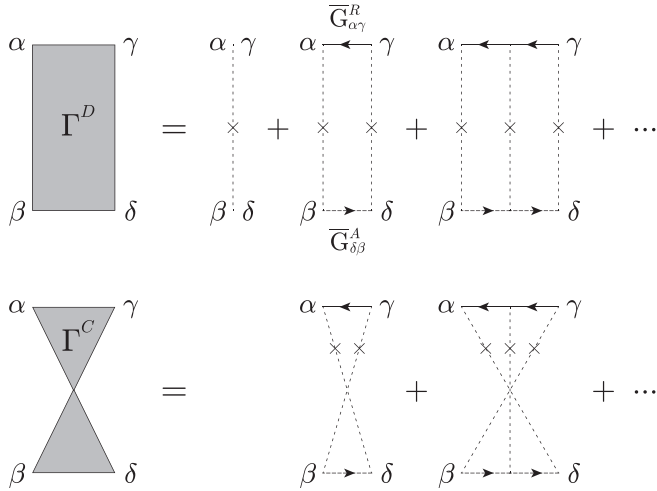


FIG. 5. Diffuson and cooperon diagrams. The solid line arrows and dashed line arrows represent the disorder-averaged retarded Green's function and advanced Green's function, respectively. The cross marks and dotted lines represent interactions with impurities. The subscripts correspond to Eqs. (35) and (36).

where

$$\Pi_1(\varepsilon, \omega) = \frac{1}{4} \int \frac{d^2 \mathbf{k}''}{(2\pi)^2} \left[g_+^R(\mathbf{k}'', \varepsilon + \frac{\omega}{2}) + g_-^R(\mathbf{k}'', \varepsilon + \frac{\omega}{2}) \right] \times \left[g_+^A(\mathbf{k}'', \varepsilon - \frac{\omega}{2}) + g_-^A(\mathbf{k}'', \varepsilon - \frac{\omega}{2}) \right], \quad (43)$$

$$\Pi_2(\varepsilon, \omega) = \frac{1}{4} \int \frac{d^2 \mathbf{k}''}{(2\pi)^2} \left[g_+^R(\mathbf{k}'', \varepsilon + \frac{\omega}{2}) - g_-^R(\mathbf{k}'', \varepsilon + \frac{\omega}{2}) \right] \times \left[g_+^A(\mathbf{k}'', \varepsilon - \frac{\omega}{2}) - g_-^A(\mathbf{k}'', \varepsilon - \frac{\omega}{2}) \right]. \quad (44)$$

Substituting Eqs. (41) and (42) into the Bethe-Salpeter equations (35) and (36), we obtain

$$\Gamma^D(\mathbf{0}, \varepsilon, \omega) = \begin{pmatrix} \frac{\Gamma_1 + \Gamma_3}{2} & 0 & 0 & \frac{\Gamma_1 - \Gamma_3}{2} \\ 0 & \Gamma_2 & 0 & 0 \\ 0 & 0 & \Gamma_2 & 0 \\ \frac{\Gamma_1 - \Gamma_3}{2} & 0 & 0 & \frac{\Gamma_1 + \Gamma_3}{2} \end{pmatrix}, \quad (45)$$

$$\Gamma^C(\mathbf{0}, \varepsilon, \omega) = \begin{pmatrix} \Gamma_2 - \gamma_0 & 0 & 0 & -\frac{\Gamma_1 - \Gamma_3}{2} \\ 0 & \frac{\Gamma_1 + \Gamma_3}{2} - \gamma_0 & 0 & 0 \\ 0 & 0 & \frac{\Gamma_1 + \Gamma_3}{2} - \gamma_0 & 0 \\ -\frac{\Gamma_1 - \Gamma_3}{2} & 0 & 0 & \Gamma_2 - \gamma_0 \end{pmatrix}, \quad (46)$$

where

$$\Gamma_1(\varepsilon, \omega) = \frac{\gamma_0}{1 - \gamma_0[\Pi_1(\varepsilon, \omega) + \Pi_2(\varepsilon, \omega)]}, \quad (47)$$

$$\Gamma_2(\varepsilon, \omega) = \frac{\gamma_0}{1 - \gamma_0 \Pi_1(\varepsilon, \omega)}, \quad (48)$$

$$\Gamma_3(\varepsilon, \omega) = \frac{\gamma_0}{1 - \gamma_0[\Pi_1(\varepsilon, \omega) - \Pi_2(\varepsilon, \omega)]}. \quad (49)$$

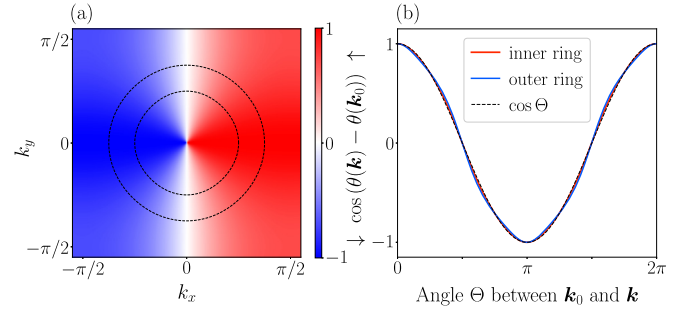


FIG. 6. (a) Value of $\cos[\theta(\mathbf{k}) - \theta(\mathbf{k}_0)]$ for $\mathbf{k}_0 = (\pi/4, 0)$. The dashed lines represent energy contours. (b) Value of $\cos[\theta(\mathbf{k}) - \theta(\mathbf{k}_0)]$ on the inner and outer rings shown as dashed lines in (a). We compare with $\cos \Theta$, where Θ is the angle between \mathbf{k} and \mathbf{k}_0 .

By transforming Γ^D and Γ^C into the \pm basis using Eqs. (32) and (33), respectively, substituting them into Eqs. (29) and (30), and rearranging Eq. (27), we obtain the disorder-averaged momentum distribution at $\mathbf{k} = -\mathbf{k}_0$,

$$n_-(-\mathbf{k}_0, t) = \int_{-\infty}^{\infty} \frac{d\varepsilon}{2\pi} \int_{-\infty}^{\infty} \frac{d\omega}{2\pi} e^{-i\omega t} \left(\frac{\Gamma_1(\varepsilon, \omega)}{2} + \Gamma_2(\varepsilon, \omega) + \frac{\Gamma_3(\varepsilon, \omega)}{2} - \gamma_0 \right) \times g_+^R(\mathbf{k}_0, \varepsilon + \frac{\omega}{2}) g_+^A(\mathbf{k}_0, \varepsilon - \frac{\omega}{2}) \times g_-^R(\mathbf{k}_0, \varepsilon + \frac{\omega}{2}) g_-^A(\mathbf{k}_0, \varepsilon - \frac{\omega}{2}), \quad (50)$$

$$n_+(-\mathbf{k}_0, t) = 0. \quad (51)$$

Since $|\mathbf{k}_0, +\rangle$ and $|\mathbf{k}_0, -\rangle$ are time-reversed states, $n_+(-\mathbf{k}_0) = 0$, which is consistent with Eq. (2). If \mathbf{k} is not close to $-\mathbf{k}_0$, the contribution of the cooperon is negligible. In this case, the disorder-averaged momentum distribution at \mathbf{k} is

$$n_{\pm}(\mathbf{k}, t) = \int_{-\infty}^{\infty} \frac{d\varepsilon}{2\pi} \int_{-\infty}^{\infty} \frac{d\omega}{2\pi} e^{-i\omega t} \{ \Gamma_1(\varepsilon, \omega) \pm \Gamma_2(\varepsilon, \omega) \cos[\theta(\mathbf{k}) - \theta(\mathbf{k}_0)] \} \times g_{\pm}^R(\mathbf{k}_0, \varepsilon + \frac{\omega}{2}) g_{\pm}^A(\mathbf{k}_0, \varepsilon - \frac{\omega}{2}) \times g_{\pm}^R(\mathbf{k}, \varepsilon + \frac{\omega}{2}) g_{\pm}^A(\mathbf{k}, \varepsilon - \frac{\omega}{2}). \quad (52)$$

Here, for the moment we ignore the terms associated with Φ_{\pm}^0 since they are zero except for $\mathbf{k} = \mathbf{k}_0$. The first term in Eq. (52) is an isotropic contribution, while the second term is an anisotropic contribution proportional to $\cos[\theta(\mathbf{k}) - \theta(\mathbf{k}_0)]$. Figure 6(a) shows how $\cos[\theta(\mathbf{k}) - \theta(\mathbf{k}_0)]$ varies with \mathbf{k} when $\mathbf{k}_0 = (\pi/4, 0)$. The dashed curves are energy contours with energy $E_+(\mathbf{k}_0)$ for the Ando model without disorder ($W = 0$) for SOC strength $\varphi = \pi/16$. In Fig. 6(b) we show the variation of the factor $\cos[\theta(\mathbf{k}) - \theta(\mathbf{k}_0)]$ along these energy contours. We see that, for the parameters considered in this paper, this factor is well approximated by $\cos \Theta$, where Θ is the angle between \mathbf{k}_0 and \mathbf{k} .

TABLE II. Roots of Eqs. (56) and (57) in the weak and strong limits of the SOC. Note that we are setting $\hbar = 1$ in this section.

ω_l	Weak SOC $\tau\Delta \ll 1$	Strong SOC $\tau\Delta \gg 1$
ω_1	$\frac{\tau\Delta^2}{2}$	$\frac{1}{2\tau}$
ω_2, ω_3	$\frac{1}{\tau} \pm i\frac{\Delta}{\sqrt{2}}$	$\frac{3}{4\tau} \pm i\Delta$
ω_4, ω_5	$\tau\Delta^2, \frac{1}{\tau}[1 - (\tau\Delta)^2]$	$\frac{1}{2\tau} \pm i\Delta$

We define Δ so that $\Delta = E_+(\mathbf{k}_0) - E_-(\mathbf{k}_0)$ and approximate Γ_1, Γ_2 , and Γ_3 by evaluating Π_1 and Π_2 in Eqs. (47)–(49) as

$$\Gamma_1(\varepsilon, \omega) \simeq \gamma_0 \frac{\omega + \frac{i}{\tau}}{\omega}, \quad (53)$$

$$\Gamma_2(\varepsilon, \omega) \simeq \gamma_0 \frac{(\omega + \frac{i}{\tau})(\omega + \Delta + \frac{i}{\tau})(\omega - \Delta + \frac{i}{\tau})}{(\omega + i\omega_1)(\omega + i\omega_2)(\omega + i\omega_3)}, \quad (54)$$

$$\Gamma_3(\varepsilon, \omega) \simeq \gamma_0 \frac{(\omega + \Delta + \frac{i}{\tau})(\omega - \Delta + \frac{i}{\tau})}{(\omega + i\omega_4)(\omega + i\omega_5)}, \quad (55)$$

where ω_1, ω_2 , and ω_3 are the roots of the cubic equation

$$\omega^3 - \frac{2}{\tau}\omega^2 + \left(\frac{1}{\tau^2} + \Delta^2\right)\omega - \frac{\Delta^2}{2\tau} = 0 \quad (56)$$

and ω_4 and ω_5 are the roots of the quadratic equation

$$\omega^2 - \frac{1}{\tau}\omega + \Delta^2 = 0. \quad (57)$$

These equations were also obtained in Ref. [39]. Note that both $\tau\omega_l$ and ω_l/Δ ($l = 1, 2, \dots, 5$) can be expressed as functions of a single variable $\tau\Delta$. Detailed calculations are given in Appendix C, but we emphasize that the method we use is not perturbative in the strength of the SOC, i.e., Eqs. (53)–(55) are a good approximation even if Δ is larger than $1/\tau$, provided Δ is sufficiently smaller than the band width. The term Γ_1 in Eq. (53) has a singularity at $\omega = 0$. Therefore, after a sufficiently long time, only the contribution from Γ_1 remains. Equation (56) has one real root, which we denote by ω_1 , and two complex conjugate roots, which we denote by ω_2 and ω_3 . All the roots have positive real parts. The two roots ω_4 and ω_5 of Eq. (57) are real when $2\tau\Delta < 1$ and complex conjugates when $2\tau\Delta > 1$. The real parts of these roots are always positive. We summarize the properties of the roots in Table II for the limits of weak and strong SOC. In the case of weak SOC, energy scales of $\tau\Delta^2$ and $1/\tau$ appear, while in the case of strong SOC, energy scales of Δ and $1/\tau$ appear. These energies correspond to the time scales tabulated in Table I.

Substituting Eqs. (53)–(55) into Eq. (50) and using the residue theorem, we obtain the disorder-averaged momentum distribution at $\mathbf{k} = -\mathbf{k}_0$,

$$n_-(-\mathbf{k}_0, t) = f\left(t, 0, \frac{1}{\tau}, \Delta\right) + 2f\left(t, \omega_1, \frac{\omega_2 + \omega_3}{2}, \frac{\omega_2 - \omega_3}{2i}\right) + g\left(t, \frac{1}{\tau}, \omega_4, \omega_5\right) - 2f\left(t, \frac{1}{\tau}, \frac{1}{\tau}, \Delta\right) \quad (58)$$

for $2\tau\Delta < 1$ and

$$n_-(-\mathbf{k}_0, t) = f\left(t, 0, \frac{1}{\tau}, \Delta\right) + 2f\left(t, \omega_1, \frac{\omega_2 + \omega_3}{2}, \frac{\omega_2 - \omega_3}{2i}\right) + f\left(t, \frac{1}{\tau}, \frac{\omega_4 + \omega_5}{2}, \frac{\omega_4 - \omega_5}{2i}\right) - 2f\left(t, \frac{1}{\tau}, \frac{1}{\tau}, \Delta\right) \quad (59)$$

for $2\tau\Delta > 1$, where

$$f(t, x, y, z) = \frac{\gamma_0}{(x-y)^2 + z^2} \left[e^{-xt} - e^{-yt} \left(\cos(zt) - \frac{x-y}{z} \sin(zt) \right) \right], \quad (60)$$

$$g(t, x, y, z) = -\frac{\gamma_0}{(x-y)(y-z)(z-x)} [(y-z)e^{-xt} + (z-x)e^{-yt} + (x-y)e^{-zt}]. \quad (61)$$

The first terms of Eqs. (58) and (59) remain at $t \rightarrow \infty$. On the other hand, substituting Eqs. (53)–(55) into Eq. (52), we obtain

$$n_{\pm}(\mathbf{k}, t) = f\left(t, 0, \frac{1}{\tau}, \tilde{\Delta}_{\pm}(\mathbf{k})\right) \pm h\left(t, \omega_1, \frac{\omega_2 + \omega_3}{2}, \frac{\omega_2 - \omega_3}{2i}, \frac{1}{\tau}, \tilde{\Delta}_{\pm}(\mathbf{k}), \frac{1}{\tau}, \Delta\right) \cos[\theta(\mathbf{k}) - \theta(\mathbf{k}_0)], \quad (62)$$

where

$$\tilde{\Delta}_{\pm}(\mathbf{k}) = E_+(\mathbf{k}_0) - E_{\pm}(\mathbf{k}) \quad (63)$$

and

$$\begin{aligned} h(t, s, u, v, w, x, y, z) = & \frac{\gamma_0 e^{-st} [(s-y)^2 + z^2]}{[(s-u)^2 + v^2][(s-w)^2 + x^2]} \\ & - \gamma_0 e^{-ut} \left[\frac{[i(y-u) + (z+v)][i(y-u) - (z-v)]e^{-ivt}}{2v[i(s-u) + v][i(w-u) + (x+v)][i(w-u) - (x-v)]} + \text{H.c.} \right] \\ & - \gamma_0 e^{-wt} \left[\frac{[i(y-w) + (z+x)][i(y-w) - (z-x)]e^{-ixt}}{2x[i(s-w) + x][i(u-w) + (v+x)][i(u-w) - (v-x)]} + \text{H.c.} \right]. \end{aligned} \quad (64)$$

TABLE III. Scattering time, spin splitting, and density of states per unit area for $\varphi = \pi/1024$, $\pi/128$, and $\pi/16$. These values are used to calculate the solid lines in Figs. 2(d)–2(f). The lattice constant is the unit of length, t_{hop} in Eq. (4) is the unit of energy, and \hbar/t_{hop} is the unit of time. The mean free path $l_e = v\tau$, where v is the group velocity, is not used in the calculation. We note that $k_0 l_e \gg 1$ for the parameters considered in our simulations.

Parameter \ φ	$\pi/1024$	$\pi/128$	$\pi/16$
SOC strength $\tau \Delta/\hbar$	0.194	1.55	11.8
Spin splitting Δ	8.68×10^{-3}	0.0694	0.552
Scattering time τ	22.34	22.40	21.31
Mean free path l_e	31.7	32.4	35.4
Density of states ρ	0.1713	0.1721	0.1806

Also, when $\mathbf{k} = \mathbf{k}_0$, there is an additional contribution

$$\int_{-\infty}^{\infty} \frac{d\varepsilon}{2\pi} \int_{-\infty}^{\infty} \frac{d\omega}{2\pi} e^{-i\omega t} \Phi_{\pm}^0(\mathbf{k}, \varepsilon, \omega) = e^{-t/\tau} \delta(\mathbf{k} - \mathbf{k}_0) \delta_{\pm,+}. \quad (65)$$

The discussion up to this point can be carried out in the same manner when the initial state is $|\mathbf{k}_0, -\rangle$.

The diagrammatic calculation presented above is valid for weak disorder. More precisely, the condition is that $k_F l_e \gg 1$, where k_F is the Fermi wave vector and l_e is the mean free path. In addition, the time scales under consideration should be not too long. The relevant time scales here are the Thouless time $\tau_D = L^2/D$, where L is the system size and $D = v^2\tau/2$ is the diffusion constant (with v the group velocity), and the localization time $\tau_{\text{loc}} = \xi^2/D$, where ξ is the localization length. For times longer than the shorter of these two time scales, a coherent forward scattering peak [12] is expected. The diffuson and the cooperon are not sufficient to capture this phenomenon.

IV. RESULTS

We performed simulations of the time evolution of a wave packet using the two-dimensional Ando model (4) defined on an $L \times L$ lattice with $L = 512$ and periodic boundary conditions. We used the Chebyshev expansion method [40] to calculate the time evolution of the state vector. The initial state was a plane wave (25) with a wave vector of $\mathbf{k}_0 = (\pi/4, 0)$. We considered three different values for the Ando model parameter φ : $\pi/1024$, $\pi/128$, and $\pi/16$. In each case, we fixed the disorder strength at $W = 1$ and estimated the average of the momentum distribution by sampling $2^{13} = 8192$ disorder realizations. We used the coherent potential approximation [41] to estimate the density of states, scattering time, and mean free path for these parameters. The values are given in Table III together with the spin splitting Δ and the value of the dimensionless ratio $\tau \Delta/\hbar$.

We focus first on the time dependence of the disorder-averaged momentum distribution $n(\mathbf{k}, t)$ at $\mathbf{k} = -\mathbf{k}_0$, which is parallel to the backscattering direction. In Figs. 2(a)–2(c) we plot $n(-\mathbf{k}_0, t)$ obtained from our simulations. For comparison we also plot $n(\mathbf{k}, t)$ at $\mathbf{k} = (0, \pi/4)$, which is orthogonal to the backscattering direction. For weak SOC [Fig. 2(a)], $n(-\mathbf{k}_0, t)$

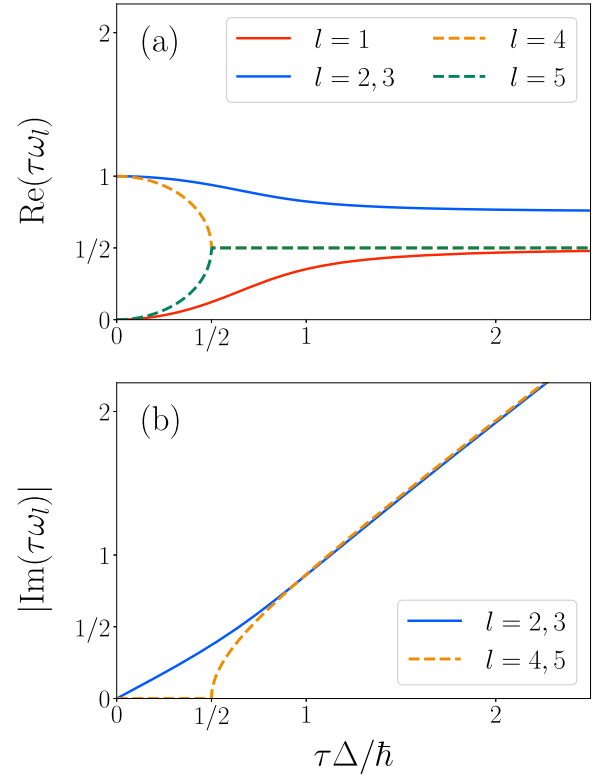


FIG. 7. SOC strength Δ dependence of the roots ω_l ($l = 1, 2, \dots, 5$) of Eqs. (56) and (57) for (a) real part of ω_l and (b) the absolute value of the imaginary part. The solid lines represent the roots of Eq. (56) [$\text{Re}(\omega_1) < \text{Re}(\omega_2) = \text{Re}(\omega_3)$] and the dashed lines represent the roots of Eq. (57). For convenience, we define $\text{Re}(\omega_4) \geq \text{Re}(\omega_5)$. We make the abscissa and ordinate dimensionless by multiplying by the scattering time τ . Note that $\tau \omega_l$ is a function of a single variable $\tau \Delta/\hbar$.

increases from zero and peaks at approximately twice the diffusive background on a time scale of the order of several scattering times, i.e., for short times this behavior is similar to the CBS observed in the absence of SOC. After this, however, there is a crossover to decreasing behavior with a limiting value of $n(-\mathbf{k}_0, t)$ equal to half the diffusive background at long times. For intermediate SOC strength [Fig. 2(b)], we see that $n(-\mathbf{k}_0, t)$ still exhibits a maximum at short times and at longer times tends to a limiting value that is a small fraction of the diffusive background. For strong SOC [Fig. 2(c)], we see that $n(-\mathbf{k}_0, t)$ is greatly reduced compared to the diffusive background, exhibits decaying oscillations, and tends to a constant value at long times.

In Figs. 2(d)–2(f) we overlay the disorder-averaged momentum distribution at $\mathbf{k} = -\mathbf{k}_0$ obtained from simulations with calculations of Eq. (58) or (59) with values of the scattering time τ and the spin splitting Δ given in Table III. The analytical equations and the simulation results exhibit clear and consistent agreement for weak, intermediate, and strong SOC. This demonstrates that considering only the diffuson and the cooperon provides a good approximation for the disorder-averaged momentum distribution.

The time scales governing the behavior of $n(-\mathbf{k}_0, t)$ are determined by the roots ω_l ($l = 1, 2, \dots, 5$) of Eqs. (56) and (57). In Fig. 7 we show the SOC strength Δ dependence of the

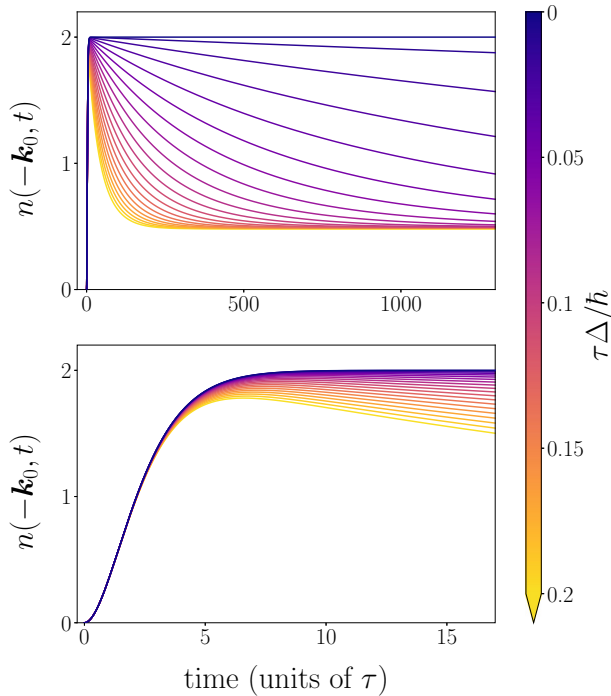


FIG. 8. Time evolution of the disorder-averaged momentum distribution at $\mathbf{k} = -\mathbf{k}_0$ for various values of $\tau\Delta/\hbar$ (from 0 to 0.2 with intervals of 0.01) in the weak SOC regime obtained from the diagrammatic calculation, i.e., Eq. (58). The short-time behavior is shown in the bottom figure. The disorder-averaged momentum distribution is expressed in units of $2\tau/\pi\hbar\rho$, the height of the diffusive background in the absence of SOC. This value differs by a factor of 2, corresponding to the spin degrees of freedom, compared to that of Ref. [20].

roots. From Eqs. (58) and (59) it is evident that the reciprocals of the real parts of the roots determine the overall time dependence of $n(-\mathbf{k}_0, t)$. If a root is a complex number, it signifies that the associated terms exhibit damped oscillations with the imaginary part of the root giving the associated frequency of oscillation. The term that gives the dominant contribution varies with the parameters of the system and with time. To understand qualitatively the behavior of $n(-\mathbf{k}_0, t)$, we focus on two extremes: the limit where the SOC is weak compared to disorder and the limit where it is strong.

For weak SOC, the enhancement of backscattering by a factor of 2 compared to the diffusive background appears at a time scale of several τ , while the subsequent reduction to one half of the diffusive background, which is shown in Fig. 8, occurs on a much longer time scale of

$$\frac{\hbar^2}{\tau\Delta^2} = \left(\frac{\tau_p}{\tau}\right)^2 \tau, \quad (66)$$

where

$$\tau_p = \frac{\hbar}{\Delta} \quad (67)$$

is the spin precession time.

For strong SOC, two diffusive rings appear because of the spin splitting due to the SOC. The width of the rings, which is of order \hbar/τ , is small compared with their splitting, which is of order $\delta k \approx \Delta/\hbar v$, where v is the average of the

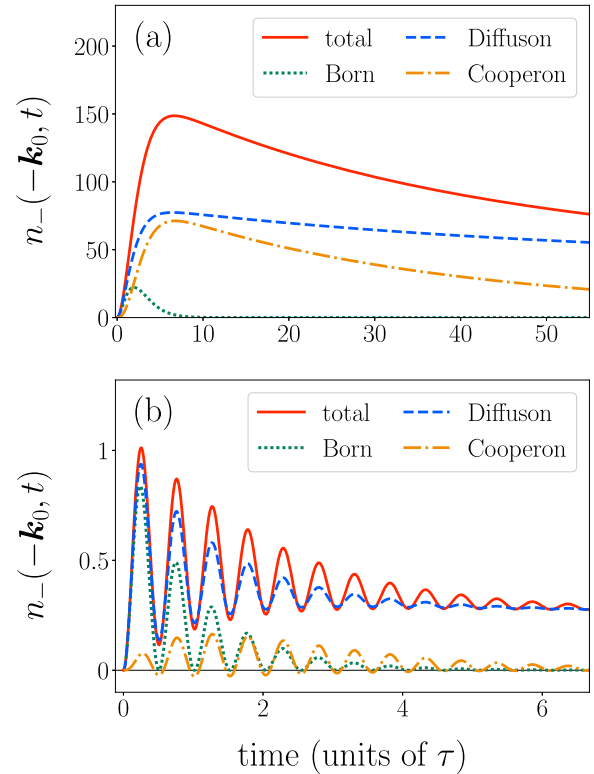


FIG. 9. Disorder-averaged momentum distribution at $\mathbf{k} = -\mathbf{k}_0$ decomposed into the contributions from single scattering (Born approximation), diffuson, and cooperon, for (a) $\varphi = \pi/1024$ and (b) $\varphi = \pi/16$. Note that we define the diffuson to include the lowest-order diagram. The solid lines labeled “total” correspond to the solid lines in Figs. 2(d) and 2(f).

group velocities at \mathbf{k}_0 . The oscillations that are shown in Fig. 2(f) arise from the diffuson and cooperon contributions to $n_-(-\mathbf{k}_0, t)$. At $\mathbf{k} = -\mathbf{k}_0$, $n_+(-\mathbf{k}_0, t) = 0$ holds exactly for all t . The period of oscillation coincides with the spin precession time τ_p .

While the contributions of the diffuson and cooperon at $\mathbf{k} = -\mathbf{k}_0$ cannot be separated in the simulation, they can be separated analytically. The contributions of the diffuson and cooperon to $n_+(-\mathbf{k}_0, t)$ are equal in magnitude but opposite in sign and cancel exactly. In Fig. 9 we investigate the contributions to $n_-(-\mathbf{k}_0, t)$ of the diffuson and cooperon for both weak and strong SOC. In both cases, the short-time behavior can be explained by the expression derived from the single-scattering diagram (Born approximation). However, beyond the scattering time τ , the contribution of multiple scattering becomes important. Oscillations of $n_-(-\mathbf{k}_0, t)$ gradually decay, but the oscillations originating from the cooperon persist longer than those originating from the diffuson.

We now shift our attention to the time dependence of the disorder-averaged momentum distribution at other momenta $\mathbf{k} \neq -\mathbf{k}_0$. The initial state is spin polarized and there is consequently a resulting anisotropy in the disorder-averaged momentum distribution. This relaxes to an isotropic distribution only at sufficiently long times as a result of spin relaxation. By investigating this we determine the spin-relaxation time for both weak and strong SOC. For strong

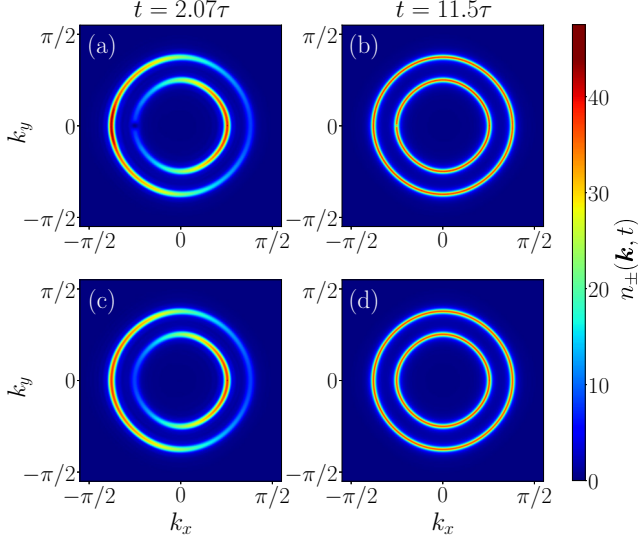


FIG. 10. Disorder-averaged momentum distribution in the strong SOC regime ($\varphi = \pi/16$) for $\mathbf{k}_0 = (\pi/4, 0)$. Simulation results are at times (a) $t = 2.07\tau$ and (b) $t = 11.5\tau$ and analytical results at times (c) $t = 2.07\tau$ and (d) $t = 11.5\tau$. At $t = 2.07\tau$, the disorder-averaged momentum distribution exhibits an anisotropic pattern, while at $t = 11.5\tau$, it becomes isotropic, except at $\mathbf{k} = -\mathbf{k}_0$.

SOC two diffusive rings are well resolved as a result of the spin splitting due to SOC. These are clearly visible in Fig. 3 and also in Figs. 10 and 11. In Fig. 10 we compare the disorder-averaged momentum distribution obtained from simulations with those calculated using Eq. (62). In Figs. 10(a) and 10(b) we present the results of the simulations, while in Figs. 10(c) and 10(d) we present the results of the analytical calculations. In Fig. 11 we present cross-sectional views of Figs. 10(a) and 10(c) along the k_x and k_y axes, respectively.

For weak SOC the spin splitting is small, the two diffusive rings overlap, and this anisotropy is hidden. It is revealed, however, when the disorder-averaged momentum distribution is resolved into $+$ and $-$ components as in Fig. 12.

Comparing the results of the simulations with the analytical calculations, it is evident that the behavior of the diffusive background can be explained using the diffuson. The cooperon contributes only in the vicinity of $\mathbf{k} = -\mathbf{k}_0$. The anisotropy in the disorder-averaged momentum distribution arises from the second term in Eq. (62). By examining the sign of this second term, we can deduce that intrabranch scattering is more likely to occur at small angles with respect to the initial wave vector than interbranch scattering. Conversely, interbranch scattering is more likely to occur at large angles. The second term in Eq. (62) decays exponentially in the long-time limit; as a result, the imbalance between the components of the two branches vanishes in that limit. This corresponds precisely to the process of spin relaxation. The function h given in Eq. (64) decays at three different time scales, namely, τ ,

$$\tau_1 = \frac{1}{\omega_1}, \quad \tau_2 = \frac{1}{\text{Re}(\omega_2)} = \frac{1}{\text{Re}(\omega_3)}. \quad (68)$$

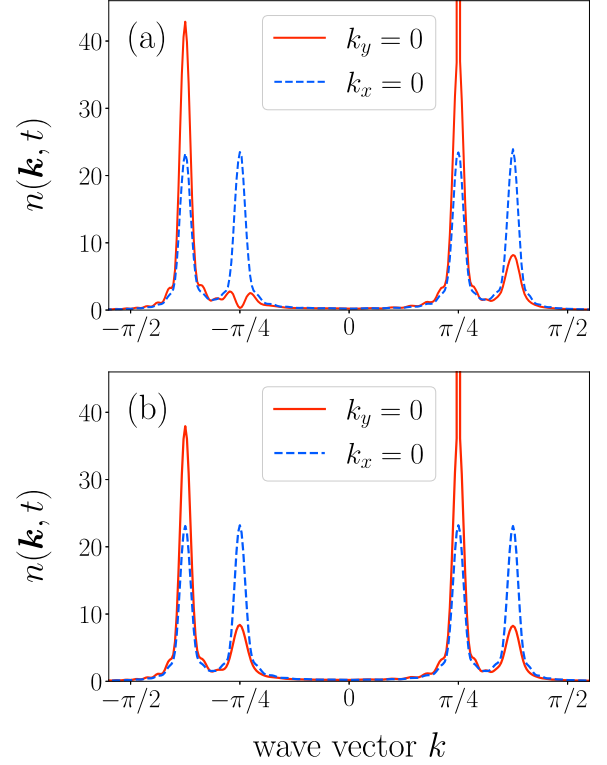


FIG. 11. Disorder-averaged momentum distribution at time $t = 2.07\tau$ plotted along the k_x axis (red solid line) and the k_y axis (blue dashed line). (a) Simulation results. (b) Analytical results. These figures correspond to Figs. 10(a) and 10(c), respectively. The analytical calculation, considering only the diffuson, is in agreement with the numerical simulation results, except at $\mathbf{k} = -\mathbf{k}_0$.

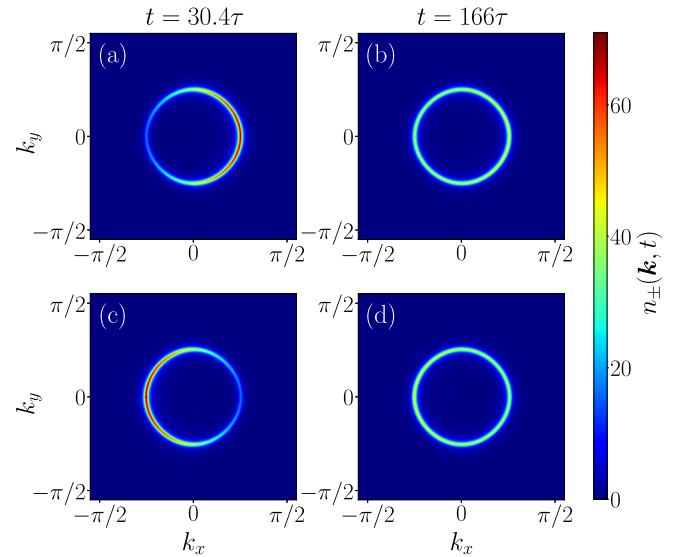


FIG. 12. Disorder-averaged momentum distribution resolved into $+$ and $-$ components for weak SOC ($\varphi = \pi/1024$) for $\mathbf{k}_0 = (\pi/4, 0)$ obtained in simulations. The $+$ component $n_+(\mathbf{k})$ is shown at times (a) $t = 30.4\tau$ and (b) $t = 166\tau$ and the $-$ component $n_-(\mathbf{k})$ at times (c) $t = 30.4\tau$ and (d) $t = 166\tau$. The total distribution $n(\mathbf{k}) = n_-(\mathbf{k}) + n_+(\mathbf{k})$ appears isotropic even at $t = 30.4\tau$, even though each component is anisotropic.

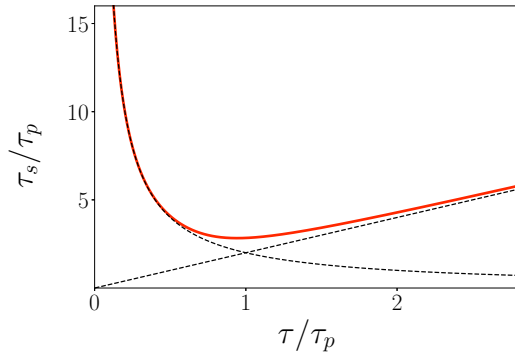


FIG. 13. Dependence of the spin-relaxation time τ_s on the scattering time τ . We make the abscissa and ordinate dimensionless by dividing them by the spin precession time $\tau_p = \hbar/\Delta$. Note that τ_s/τ_p is a function of a single variable τ/τ_p . The dashed lines show $2\tau_p/\tau$ and $2\tau/\tau_p$, respectively.

Since the equilibration of the spin imbalance occurs on the slowest time scale, we conclude that the spin-relaxation time is given by $\tau_s = \tau_1$.

In Fig. 13 we show the dependence of the spin-relaxation time τ_s on τ . For weak SOC, the spin-relaxation time is inversely proportional to the scattering time. This behavior is consistent with the D'yakonov-Perel' spin-relaxation mechanism [42,43]. For strong SOC, we find Elliott-Yafet-like behavior with the spin-relaxation time proportional to τ [44,45]. The τ dependence of τ_s shown in Fig. 13 provides a quantitative description of the crossover between these two regimes of spin relaxation.

V. DISCUSSION

We have investigated, both numerically and analytically, the time evolution of a particle in an initial plane-wave state as it propagates coherently in a two-dimensional disordered system with SOC. We have focused in particular on the time dependence of backscattering and the time dependence of the anisotropy of the diffusive background. We have found that the results of our numerical simulations are well described by analytic calculations that treat the SOC nonperturbatively and the effects of disorder using the diffuson and cooperon.

For weak SOC, we find at short times of the order of a few times the scattering time τ an enhancement of backscattering by a factor of 2 relative to the diffusive background. This factor of 2 is characteristic of CBS in systems without SOC. With SOC, however, for longer times, of the order of $(\tau_p/\tau)^2\tau$, there is crossover to a reduction of backscattering by a factor of $\frac{1}{2}$, which is characteristic of CBS in systems with SOC.

With SOC, the spin polarization of the initial plane-wave state is reflected in an anisotropy of the disorder-averaged momentum distribution. This anisotropy relaxes on the time scale of the spin-relaxation time τ_s and we have taken advantage of this to calculate the spin-relaxation time. For weak SOC, we have found a spin-relaxation time that is inversely proportional to the scattering time τ consistent with the D'yakonov-Perel' spin-relaxation mechanism. For strong SOC, we have found an Elliott-Yafet-like behavior with the

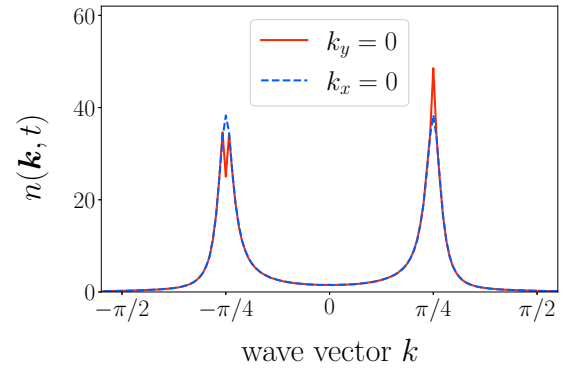


FIG. 14. Disorder-averaged momentum distribution at time $t = 1492\tau$ estimated by sampling 8192 disorder realizations for $\mathbf{k}_0 = (\pi/4, 0)$. The time t is sufficiently longer than the Thouless time $\tau_D \simeq 648\tau$ that a CFS peak is observed.

spin-relaxation time proportional to τ . Our analytic calculations describe quantitatively the crossover between these two regimes. Our results are consistent with those reported in Ref. [39].

The effects we discuss theoretically in this paper should be observable in a cold atomic gas with synthetic SOC. For simplicity, we have studied a model from solid-state physics with an uncorrelated potential. For easier comparison with experiments with cold atoms, it may be important in future work to extend our calculations by using a speckle potential. It should be noted though that correlations of a realistic speckle potential impose a considerable burden in numerical simulations [46,47]. While taking account of these correlations is necessary, for example, for an accurate quantitative determination of the mobility edge at which the Anderson transition occurs, we think the calculations we report do yield considerable insight. Also, in systems with correlated disorder, such as a speckle potential, an anisotropy of the diffusive background emerges naturally [20,48]. However, in this study, the random potential is uncorrelated and the anisotropy is purely a result of the SOC.

In the Anderson localized phase a coherent forward scattering (CFS) peak emerges in the disorder-averaged momentum distribution at $\mathbf{k} = \mathbf{k}_0$ at sufficiently long times [12,32]. Even in the metallic regime or in regimes where the localization length is sufficiently long compared to the system size L , a CFS peak also manifests as an effect of finite size [37]. The relevant time scale is the Thouless time. For the Ando model with $L = 512$, $W = 1$, and $\varphi = \pi/1024$, the estimated Thouless time is approximately $\tau_D \simeq 522\tau$. Therefore, no CFS peak is expected or observed in the simulations we reported above. When simulating smaller systems and longer times, a CFS peak appears. In Fig. 14 we show the CFS peak observed in a simulation of the Ando model with $L = 256$, $W = 1.5$, and $\varphi = \pi/1024$. For these parameters, using the coherent potential approximation, we estimate $\tau = 10.03$ in units of \hbar/t_{hop} .

Finally, we have considered the noninteracting limit. The effects of interactions on coherent propagation in cold atoms have also been studied [38,49,50] using the Gross-Pitaevskii equation.

ACKNOWLEDGMENTS

K.S. is grateful for support from the Japan Society for the Promotion of Science under Grant-in-Aid No. 19H00658. K.S. thanks S. Kettemann, G. Lemarié, and C. Minatura for helpful discussions.

APPENDIX A: PROBABILITY AMPLITUDE FOR SCATTERING INTO A TIME-REVERSED STATE

We recall some basic definitions and properties based on Ref. [51]. For any two states $|\phi\rangle$ and $|\psi\rangle$ we have

$$\langle\phi|\psi\rangle = \langle\psi|\phi\rangle^*. \quad (\text{A1})$$

The Hermitian conjugate of an operator A is the operator A^\dagger such that

$$\langle\phi|A\psi\rangle = \langle A^\dagger\phi|\psi\rangle \quad (\text{A2})$$

for all states $|\phi\rangle$ and $|\psi\rangle$ satisfying the appropriate boundary conditions. Time-reversal operators are antiunitary. The defining property of an antiunitary operator is

$$\langle T\phi|T\psi\rangle = \langle\psi|\phi\rangle. \quad (\text{A3})$$

The time-evolution operator for the system described by a time-independent Hamiltonian H is

$$U(t) = \exp(-iHt), \quad (\text{A4})$$

where t is time. Since any time-reversal operator can be expressed as a product of a unitary operator and complex conjugation in a suitable basis, assuming that

$$[H, T] = 0, \quad (\text{A5})$$

we see that

$$TU(t) = U^\dagger(t)T. \quad (\text{A6})$$

We now consider the matrix element $\langle T\psi|U(t)\psi\rangle$. Since $T^2 = -1$, this is equal to $-\langle T\psi|T^2U(t)\psi\rangle$. Using Eq. (A6), this is then equal to $-\langle T\psi|TU^\dagger(t)T\psi\rangle$. Since T is antiunitary, this is equal to $-\langle U^\dagger(t)T\psi|\psi\rangle$. Using the definition of the Hermitian conjugate, this is equal to $-\langle T\psi|U(t)\psi\rangle$. Thus, we have found that

$$\langle T\psi|U(t)\psi\rangle = -\langle T\psi|U(t)\psi\rangle. \quad (\text{A7})$$

So the probability amplitude must be zero. An alternative derivation that makes explicit use of the Kramers degeneracy is given in Ref. [32].

APPENDIX B: DISORDER-AVERAGED GREEN'S FUNCTION OF THE ANDO MODEL

The retarded free Green's function of the Ando model in the \pm basis can be calculated using Eq. (14),

$$G_0^R(\mathbf{k}, \varepsilon) = g_{0+}^R(\mathbf{k}, \varepsilon)|\mathbf{k}, +\rangle\langle\mathbf{k}, +| + g_{0-}^R(\mathbf{k}, \varepsilon)|\mathbf{k}, -\rangle\langle\mathbf{k}, -|, \quad (\text{B1})$$

where $g_{0\pm}^R$ is

$$g_{0\pm}^R(\mathbf{k}, \varepsilon) = \frac{1}{\varepsilon - E_{\pm}(\mathbf{k}) + i\delta}. \quad (\text{B2})$$

Taking into account the relationship between the spin basis and the \pm basis given by Eqs. (9) and (10), the free retarded Green's function in the spin basis is expressed as

$$G_0^R(\mathbf{k}, \varepsilon) = \frac{1}{2} \begin{pmatrix} g_{0+}^R(\mathbf{k}, \varepsilon) + g_{0-}^R(\mathbf{k}, \varepsilon) & -e^{-i\theta(\mathbf{k})}[g_{0+}^R(\mathbf{k}, \varepsilon) - g_{0-}^R(\mathbf{k}, \varepsilon)] \\ -e^{i\theta(\mathbf{k})}[g_{0+}^R(\mathbf{k}, \varepsilon) - g_{0-}^R(\mathbf{k}, \varepsilon)] & g_{0+}^R(\mathbf{k}, \varepsilon) + g_{0-}^R(\mathbf{k}, \varepsilon) \end{pmatrix}. \quad (\text{B3})$$

Within the scope of the Born approximation, the self-energy in the spin basis is

$$\begin{aligned} \Sigma^R(\mathbf{k}, \mathbf{k}', \varepsilon) &= \frac{1}{L^2} \sum_{\mathbf{k}''} \overline{V(\mathbf{k}, \mathbf{k}'')G_0^R(\mathbf{k}'', \varepsilon)V(\mathbf{k}'', \mathbf{k}')} \\ &= \frac{1}{L^2} \sum_{\mathbf{k}''} \overline{V(\mathbf{k}, \mathbf{k}'')V(\mathbf{k}'', \mathbf{k}')G_0^R(\mathbf{k}'', \varepsilon)}, \end{aligned} \quad (\text{B4})$$

where $V(\mathbf{k}, \mathbf{k}')$ is a 2×2 scalar matrix with

$$V_{\sigma\sigma'}(\mathbf{k}, \mathbf{k}') = V(\mathbf{k} - \mathbf{k}')\delta_{\sigma,\sigma'} \quad (\text{B5})$$

as elements. Taking the disorder average, we obtain

$$\overline{V(\mathbf{k}, \mathbf{k}'')V(\mathbf{k}'', \mathbf{k}')} = \gamma(\mathbf{k} - \mathbf{k}'')\delta_{\mathbf{k},\mathbf{k}''}I_2. \quad (\text{B6})$$

Assuming that the random potential exhibits short-range correlations, we can take $\gamma(\mathbf{k})$ as a constant γ_0 . Since $g_{0\pm}^R(-\mathbf{k}, \varepsilon) = g_{0\pm}^R(\mathbf{k}, \varepsilon)$ and $e^{i\theta(-\mathbf{k})} = -e^{i\theta(\mathbf{k})}$, when we perform the integration in Eq. (B4), the off-diagonal elements cancel out and we find that the self-energy $\Sigma^R(\mathbf{k}, \varepsilon)$ is a scalar

matrix with imaginary part

$$\begin{aligned} \text{Im}[\Sigma^R(\mathbf{k}, \varepsilon)] &= \frac{\gamma_0}{L^2} \sum_{\mathbf{k}''} \frac{\text{Im}[g_{0+}^R(\mathbf{k}'', \varepsilon)] + \text{Im}[g_{0-}^R(\mathbf{k}'', \varepsilon)]}{2} I_2 \\ &= -\frac{\pi}{2} \gamma_0 \rho(\varepsilon) I_2. \end{aligned} \quad (\text{B7})$$

Here, $\rho(\varepsilon)$ is the density of states per unit area

$$\begin{aligned} \rho(\varepsilon) &= \frac{1}{L^2} \sum_{\mathbf{k}''} \text{Tr} \left[-\frac{1}{\pi} \text{Im} \{ G_0^R(\mathbf{k}'', \varepsilon) \} \right] \\ &= -\frac{1}{\pi L^2} \sum_{\mathbf{k}''} [\text{Im} \{ g_{0+}^R(\mathbf{k}'', \varepsilon) \} + \text{Im} \{ g_{0-}^R(\mathbf{k}'', \varepsilon) \}]. \end{aligned} \quad (\text{B8})$$

The scattering time is defined as the reciprocal of the imaginary part of the self-energy, thus

$$\text{Im} \{ \Sigma^R(\mathbf{k}, \varepsilon) \} = \frac{1}{2\tau} I_2 \quad (\text{B9})$$

Since $\Sigma^R(\mathbf{k}, \varepsilon)$ is a scalar matrix, it is unchanged when transforming to the \pm basis. As a result, the disorder-averaged Green's function in the \pm basis is also given by Eq. (18).

APPENDIX C: DERIVATION OF APPROXIMATIONS OF Γ_1 , Γ_2 , AND Γ_3

We define $E(\mathbf{k})$ and $\Delta(\mathbf{k})$ from the two energy eigenvalues in the Ando model,

$$\begin{aligned} E_{\pm}(\mathbf{k}) &= -2t_1(\cos k_x + \cos k_y) \\ &\quad \pm 2t_2\sqrt{\sin^2 k_x + \sin^2 k_y} \\ &:= E(\mathbf{k}) \pm \frac{\Delta(\mathbf{k})}{2}. \end{aligned} \quad (\text{C1})$$

In the integration we approximate Δ , ν , and τ as constants. Then using the residue theorem, we obtain

$$\begin{aligned} &\int \frac{d^2\mathbf{k}''}{(2\pi)^2} g_+^R\left(\mathbf{k}'', \varepsilon + \frac{\omega}{2}\right) g_+^A\left(\mathbf{k}'', \varepsilon - \frac{\omega}{2}\right) \\ &\simeq \int \frac{\nu dE}{(\varepsilon - E - \frac{\Delta}{2} + \frac{\omega}{2} + \frac{i}{2\tau})(\varepsilon - E - \frac{\Delta}{2} - \frac{\omega}{2} - \frac{i}{2\tau})} \\ &= \frac{2\pi i\nu}{\omega + \frac{i}{\tau}}, \end{aligned} \quad (\text{C2})$$

$$\begin{aligned} &\int \frac{d^2\mathbf{k}''}{(2\pi)^2} g_-^R\left(\mathbf{k}'', \varepsilon + \frac{\omega}{2}\right) g_-^A\left(\mathbf{k}'', \varepsilon - \frac{\omega}{2}\right) \\ &\simeq \frac{2\pi i\nu}{\omega + \frac{i}{\tau}}, \end{aligned} \quad (\text{C3})$$

$$\begin{aligned} &\int \frac{d^2\mathbf{k}''}{(2\pi)^2} g_+^R\left(\mathbf{k}'', \varepsilon + \frac{\omega}{2}\right) g_-^A\left(\mathbf{k}'', \varepsilon - \frac{\omega}{2}\right) \\ &\simeq \frac{2\pi i\nu}{\omega + \Delta + \frac{i}{\tau}}, \end{aligned} \quad (\text{C4})$$

$$\begin{aligned} &\int \frac{d^2\mathbf{k}''}{(2\pi)^2} g_-^R\left(\mathbf{k}'', \varepsilon + \frac{\omega}{2}\right) g_+^A\left(\mathbf{k}'', \varepsilon - \frac{\omega}{2}\right) \\ &\simeq \frac{2\pi i\nu}{\omega - \Delta + \frac{i}{\tau}}. \end{aligned} \quad (\text{C5})$$

Using Eqs. (C2)–(C5), we can calculate approximations for Π_1 and Π_2 from Eqs. (43) and (44). Substituting them into Eqs. (47)–(49), their denominators are

$$\begin{aligned} &1 - \gamma_0(\Pi_0 + \Pi_1) \\ &= 1 - \frac{1}{2} \int \frac{d^2\mathbf{k}''}{(2\pi)^2} \left[g_+^R\left(\mathbf{k}'', \varepsilon + \frac{\omega}{2}\right) g_+^A\left(\mathbf{k}'', \varepsilon - \frac{\omega}{2}\right) \right. \\ &\quad \left. + g_-^R\left(\mathbf{k}'', \varepsilon + \frac{\omega}{2}\right) g_-^A\left(\mathbf{k}'', \varepsilon - \frac{\omega}{2}\right) \right] \\ &\simeq 1 - \frac{\frac{i}{\tau}}{\omega + \frac{i}{\tau}} = \frac{\omega}{\omega + \frac{i}{\tau}}, \end{aligned} \quad (\text{C6})$$

$$\begin{aligned} &1 - \gamma_0\Pi_0 \\ &\simeq \frac{1}{4} \left(\frac{\omega + \Delta}{\omega + \Delta + \frac{i}{\tau}} + \frac{\omega - \Delta}{\omega - \Delta + \frac{i}{\tau}} + \frac{2\omega}{\omega + \frac{i}{\tau}} \right) \\ &= \frac{(\omega + i\omega_1)(\omega + i\omega_2)(\omega + i\omega_3)}{(\omega + \frac{i}{\tau})(\omega + \Delta + \frac{i}{\tau})(\omega - \Delta + \frac{i}{\tau})}, \end{aligned} \quad (\text{C7})$$

$$\begin{aligned} &1 - \gamma_0(\Pi_0 - \Pi_1) \\ &\simeq \frac{1}{2} \left(\frac{\omega + \Delta}{\omega + \Delta + \frac{i}{\tau}} + \frac{\omega - \Delta}{\omega - \Delta + \frac{i}{\tau}} \right) \\ &= \frac{(\omega + i\omega_4)(\omega + i\omega_5)}{(\omega + \Delta + \frac{i}{\tau})(\omega - \Delta + \frac{i}{\tau})}. \end{aligned} \quad (\text{C8})$$

Thus, we obtain Eqs. (53)–(55).

-
- [1] F. Jendrzejewski, K. Müller, J. Richard, A. Date, T. Plisson, P. Bouyer, A. Aspect, and V. Josse, Coherent backscattering of ultracold atoms, *Phys. Rev. Lett.* **109**, 195302 (2012).
- [2] G. Labeyrie, T. Karpiuk, J.-F. Schaff, B. Grémaud, C. Miniatura, and D. Delande, Enhanced backscattering of a dilute Bose-Einstein condensate, *Europhys. Lett.* **100**, 66001 (2012).
- [3] J. Billy, V. Josse, Z. Zuo, A. Bernard, B. Hambrecht, P. Lugan, D. Clément, L. Sanchez-Palencia, P. Bouyer, and A. Aspect, Direct observation of Anderson localization of matter waves in a controlled disorder, *Nature (London)* **453**, 891 (2008); the following paper demonstrates Anderson localization using a quasiperiodic optical lattice: G. Roati, C. D'Errico, L. Fallani, M. Fattori, C. Fort, M. Zaccanti, G. Modugno, M. Modugno, and M. Inguscio, Anderson localization of a non-interacting Bose-Einstein condensate, *ibid.* **453**, 895 (2008).
- [4] S. S. Kondov, W. R. McGehee, J. J. Zirbel, and B. DeMarco, Three-dimensional Anderson localization of ultracold matter, *Science* **334**, 66 (2011).
- [5] F. Jendrzejewski, A. Bernard, K. Müller, P. Cheinet, V. Josse, M. Piraud, L. Pezzé, L. Sanchez-Palencia, A. Aspect, and P. Bouyer, Three-dimensional localization of ultracold atoms in an optical disordered potential, *Nat. Phys.* **8**, 398 (2012).
- [6] B. Lecoutre, Y. Guo, X. Yu, M. Niranjan, M. Mukhtar, V. V. Volchkov, A. Aspect, and V. Josse, Bichromatic state-dependent disordered potential for Anderson localization of ultracold atoms, *Eur. Phys. J. D* **76**, 218 (2022).
- [7] J. Chabé, G. Lemarié, B. Grémaud, D. Delande, P. Szriftgiser, and J. C. Garreau, Experimental observation of the Anderson metal-insulator transition with atomic matter waves, *Phys. Rev. Lett.* **101**, 255702 (2008).
- [8] M. Lopez, J.-F. Clément, P. Szriftgiser, J. C. Garreau, and D. Delande, Experimental test of universality of the Anderson transition, *Phys. Rev. Lett.* **108**, 095701 (2012).
- [9] G. Lemarié, B. Grémaud, and D. Delande, Universality of the Anderson transition with the quasiperiodic kicked rotor, *Europhys. Lett.* **87**, 37007 (2009).

- [10] K. Slevin and T. Ohtsuki, Corrections to scaling at the Anderson transition, *Phys. Rev. Lett.* **82**, 382 (1999).
- [11] K. Slevin and T. Ohtsuki, Critical exponent for the Anderson transition in the three-dimensional orthogonal universality class, *New J. Phys.* **16**, 015012 (2014).
- [12] T. Karpiuk, N. Cherroret, K. L. Lee, B. Grémaud, C. A. Müller, and C. Miniatura, Coherent forward scattering peak induced by Anderson localization, *Phys. Rev. Lett.* **109**, 190601 (2012).
- [13] T. Prat, D. Delande, and N. Cherroret, Quantum boomeranglike effect of wave packets in random media, *Phys. Rev. A* **99**, 023629 (2019).
- [14] C. Hainaut, I. Manai, J.-F. Clément, J. C. Garreau, P. Szriftgiser, G. Lemarié, N. Cherroret, D. Delande, and R. Chicireanu, Controlling symmetry and localization with an artificial gauge field in a disordered quantum system, *Nat. Commun.* **9**, 1382 (2018).
- [15] R. Sajjad, J. L. Tanlimco, H. Mas, A. Cao, E. Nolasco-Martinez, E. Q. Simmons, F. L. N. Santos, P. Vignolo, T. Macrì, and D. M. Weld, Observation of the quantum boomerang effect, *Phys. Rev. X* **12**, 011035 (2022).
- [16] Y. Kuga and A. Ishimaru, Retroreflectance from a dense distribution of spherical particles, *J. Opt. Soc. Am. A* **1**, 831 (1984).
- [17] M. P. Van Albada and A. Lagendijk, Observation of weak localization of light in a random medium, *Phys. Rev. Lett.* **55**, 2692 (1985); P.-E. Wolf and G. Maret, Weak localization and coherent backscattering of photons in disordered media, *ibid.* **55**, 2696 (1985).
- [18] G. Bayer and T. Niederdränk, Weak localization of acoustic waves in strongly scattering media, *Phys. Rev. Lett.* **70**, 3884 (1993).
- [19] G. Bergmann, Weak localization in thin films: A time-of-flight experiment with conduction electrons, *Phys. Rep.* **107**, 1 (1984).
- [20] N. Cherroret, T. Karpiuk, C. A. Müller, B. Grémaud, and C. Miniatura, Coherent backscattering of ultracold matter waves: Momentum space signatures, *Phys. Rev. A* **85**, 011604(R) (2012).
- [21] N. Cherroret, T. Scoquart, and D. Delande, Coherent multiple scattering of out-of-equilibrium interacting Bose gases, *Ann. Phys. (NY)* **435**, 168543 (2021).
- [22] S. Hikami, A. I. Larkin, and Y. Nagaoka, Spin-orbit interaction and magnetoresistance in the two dimensional random system, *Prog. Theor. Phys.* **63**, 707 (1980).
- [23] Y.-J. Lin, K. Jiménez-García, and I. B. Spielman, Spin-orbit-coupled Bose-Einstein condensates, *Nature (London)* **471**, 83 (2011).
- [24] P. Wang, Z.-Q. Yu, Z. Fu, J. Miao, L. Huang, S. Chai, H. Zhai, and J. Zhang, Spin-orbit coupled degenerate Fermi gases, *Phys. Rev. Lett.* **109**, 095301 (2012); L. W. Cheuk, A. T. Sommer, Z. Hadzibabic, T. Yefsah, W. S. Bakr, and M. W. Zwierlein, Spin-injection spectroscopy of a spin-orbit coupled Fermi gas, *ibid.* **109**, 095302 (2012).
- [25] L. Huang, Z. Meng, P. Wang, P. Peng, S.-L. Zhang, L. C. Chen, D. Li, Q. Zhou, and J. Zhang, Experimental realization of two-dimensional synthetic spin-orbit coupling in ultracold Fermi gases, *Nat. Phys.* **12**, 540 (2016).
- [26] Z. Wu, L. Zhang, W. Sun, X.-T. Xu, B.-Z. Wang, S.-C. Ji, Y. Deng, S. Chen, X.-J. Liu, and J.-W. Pan, Realization of two-dimensional spin-orbit coupling for Bose-Einstein condensates, *Science* **354**, 83 (2016).
- [27] Z.-Y. Wang, X.-C. Cheng, B.-Z. Wang, J.-Y. Zhang, Y.-H. Lu, C.-R. Yi, S. Niu, Y. Deng, X.-J. Liu, S. Chen, and J.-W. Pan, Realization of an ideal Weyl semimetal band in a quantum gas with 3D spin-orbit coupling, *Science* **372**, 271 (2021).
- [28] Y. Yue, C. A. R. Sá de Melo, and I. B. Spielman, Enhanced transport of spin-orbit-coupled Bose gases in disordered potentials, *Phys. Rev. A* **102**, 033325 (2020).
- [29] Q. Wang, W. Zhao, and L. Wen, Dynamics of kicked spin-orbit-coupled Bose-Einstein condensates, *Results Phys.* **25**, 104317 (2021).
- [30] J. Janarek, B. Grémaud, J. Zakrzewski, and D. Delande, Quantum boomerang effect in systems without time-reversal symmetry, *Phys. Rev. B* **105**, L180202 (2022).
- [31] B. Alluf and C. A. R. Sá de Melo, Controlling Anderson localization of a Bose-Einstein condensate via spin-orbit coupling and Rabi fields in bichromatic lattices, *Phys. Rev. A* **107**, 033312 (2023).
- [32] E. Arabahmadi, D. Schumayer, B. Grémaud, C. Miniatura, and D. A. W. Hutchinson, Momentum-space signatures of the Anderson transition in a symplectic, two-dimensional, disordered ultracold gas, *Phys. Rev. Res.* **6**, L012021 (2024).
- [33] J. Janarek, N. Cherroret, and D. Delande, Berezinskii approach to disordered spin systems with asymmetric scattering and application to the quantum boomerang effect, [arXiv:2307.15354](https://arxiv.org/abs/2307.15354).
- [34] T. Ando, Numerical study of symmetry effects on localization in two dimensions, *Phys. Rev. B* **40**, 5325 (1989).
- [35] E. Akkermans and G. Montambaux, *Mesoscopic Physics of Electrons and Photons* (Cambridge University Press, London, 2007).
- [36] R. C. Kuhn, C. Miniatura, D. Delande, O. Sigwarth, and C. A. Müller, Localization of matter waves in two-dimensional disordered optical potentials, *Phys. Rev. Lett.* **95**, 250403 (2005); Coherent matter wave transport in speckle potentials, *New J. Phys.* **9**, 161 (2007).
- [37] S. Ghosh, N. Cherroret, B. Grémaud, C. Miniatura, and D. Delande, Coherent forward scattering in two-dimensional disordered systems, *Phys. Rev. A* **90**, 063602 (2014).
- [38] T. Scoquart, T. Wellens, D. Delande, and N. Cherroret, Quench dynamics of a weakly interacting disordered Bose gas in momentum space, *Phys. Rev. Res.* **2**, 033349 (2020).
- [39] L. Szolnoki, A. Kiss, B. Dóra, and F. Simon, Spin-relaxation time in materials with broken inversion symmetry and large spin-orbit coupling, *Sci. Rep.* **7**, 9949 (2017).
- [40] H. Tal-Ezer and R. Kosloff, An accurate and efficient scheme for propagating the time dependent Schrödinger equation, *J. Chem. Phys.* **81**, 3967 (1984).
- [41] P. Soven, Coherent-potential model of substitutional disordered alloys, *Phys. Rev.* **156**, 809 (1967).
- [42] M. I. D'yakonov and V. I. Perel', Spin relaxation of conduction electrons in noncentrosymmetric semiconductors, *Sov. Phys. Solid State* **13**, 3023 (1972).
- [43] M. I. D'yakonov and V. Yu. Kachorovskii, Spin relaxation of two-dimensional electrons in noncentrosymmetric semiconductors, *Sov. Phys. Semicond.* **20**, 110 (1986).
- [44] R. J. Elliott, Theory of the effect of spin-orbit coupling on magnetic resonance in some semiconductors, *Phys. Rev.* **96**, 266 (1954).
- [45] Y. Yafet, g factors and spin-lattice relaxation of conduction electrons, *Solid State Phys.* **14**, 1 (1963).

- [46] D. Delande and G. Orso, Mobility edge for cold atoms in laser speckle potentials, *Phys. Rev. Lett.* **113**, 060601 (2014).
- [47] G. Orso, Anderson transition of cold atoms with synthetic spin-orbit coupling in two-dimensional speckle potentials, *Phys. Rev. Lett.* **118**, 105301 (2017).
- [48] J. Richard, L.-K. Lim, V. Denechaud, V. V. Volchkov, B. Lecoutre, M. Mukhtar, F. Jendrzejewski, A. Aspect, A. Signoles, L. Sanchez-Palencia, and V. Josse, Elastic scattering time of matter waves in disordered potentials, *Phys. Rev. Lett.* **122**, 100403 (2019).
- [49] M. Hartung, T. Wellens, C. A. Müller, K. Richter, and P. Schlagheck, Coherent backscattering of Bose-Einstein condensates in two-dimensional disorder potentials, *Phys. Rev. Lett.* **101**, 020603 (2008).
- [50] R. Chrétien and P. Schlagheck, Inversion of coherent backscattering with interacting Bose-Einstein condensates in two-dimensional disorder: A truncated Wigner approach, *Phys. Rev. A* **103**, 033319 (2021).
- [51] F. Haake, *Quantum Signatures of Chaos*, Springer Series in Synergetics Vol. 54 (Springer, Berlin, 2010), Chap. 2.